ChemComm

ROYAL SOCIETY OF CHEMISTRY

COMMUNICATION

View Article Online
View Journal | View Issue

Check for updates

Cite this: *Chem. Commun.*, 2024, **60**, 14212

Received 26th September 2024, Accepted 6th November 2024

DOI: 10.1039/d4cc05008h

rsc.li/chemcomm

Published on 06 November 2024. Downloaded on 11/20/2025 5:27:09 PM.

A MOF-derived CuO/TiO_2 photocatalyst for methanol production from CO_2 reduction in an AI-assisted continuous flow reactor†

Bhavya Jaksani,[ab] Ruchi Chauhan,[bc] Switi Dattatraya Kshirsagar,[a] Abhilash Rana,[bc] Ujjwal Pal *[ab] and Ajay K. Singh *[bc]

A CuO/TiO_2 hybrid heterostructure was successfully engineered from copper metal–organic frameworks (MOFs) using a two-step process involving solvothermal synthesis and calcination. By precisely controlling the CuO loading, this synergistic composite exhibited exceptional performance in photocatalytic CO_2 reduction. Notably, AI-assisted continuous flow experimentation achieved a record-breaking methanol production rate of 2.3 mol g^{-1} h^{-1} without the need for sacrificial agents.

The increasing global demand for fossil fuels is depleting finite resources and increasing CO_2 emissions as a major driver of climate change. This rise in atmospheric CO_2 has inspired the development of technologies to capture, store, and convert CO_2 into value-added chemicals like methanol.[1–4] Several methods such as electrochemical, thermochemical, and photochemical approaches were reported for CO_2 conversion. Photocatalytic reduction of CO_2 with affordable and abundant semiconductors like TiO_2,[5] ZrO_2,[6] ZnO,[7] and CdS[8,9] are employed with TiO_2 being the most researched. Conventional TiO_2 catalysts have low photocatalytic efficiency due to limited visible light absorption and fast charge recombination,[10] leading researchers to enhance their effectiveness through methods like metal cluster introduction, single-atom incorporation, and MOF-templated synthesis. Metal–organic frameworks (MOFs) act as versatile templates for high-performance multicomponent catalysts, with nanoscale pores and customizable linkers.[11] Calcination transforms MOFs into mesoporous structures with open diffusion pathways boosting catalytic potential.[12] In this study, a heterojunction was formed by combining a metal oxide with TiO_2 effectively reducing photogenerated electron–hole recombination. Copper MOF (CuBTC) was used as a CuO source and the resulting MOF-derived CuO integrated with TiO_2 (MCT), significantly increased surface area and reaction sites. The CuO/TiO_2 heterojunction efficiently inhibited electron–hole recombination, enhancing photocatalytic activity through rapid charge separation, migration, and effective surface reactions. The CuO/TiO_2 architecture showed excellent photocatalytic performance for CO_2-to-methanol conversion under visible light with experimental results confirming strong synergy that significantly enhanced methanol production efficiency.

The photochemical conversion of carbon dioxide to methanol has attracted significant interest due to its wide-ranging applications in the chemical, energy, and electronics sectors.[13] Despite its potential, most current photochemical catalytic methods rely on batch processes,[14,15] which face critical challenges. These include limited control over essential parameters such as temperature, pressure, light intensity, residence time, quantum efficiency, and surface-to-volume ratio *etc.* As a result, batch processes often lead to inefficiencies, higher costs, and inconsistent product quality, rendering them non-viable for large-scale applications. In contrast, artificial intelligence (AI)-controlled continuous flow chemistry offers a breakthrough solution to these limitations.[16–22] By automating the screening and optimization of reaction parameters, AI-driven systems can determine the ideal recipe for methanol production, enhancing scalability, efficiency, and product quality.[23] This advanced approach allows for real-time adjustments to key variables, ensuring precision and consistency that batch processes cannot achieve. However, a significant challenge remains: the lack of an AI-controlled continuous flow photochemical system for methanol generation. This gap presents an exciting opportunity for innovation. Our research group is eager to take on this challenge by developing a continuous flow setup guided by Bayesian optimization. This system will autonomously optimize reaction parameters to maximize methanol yield and process efficiency, providing a cutting-edge solution for sustainable and economically viable methanol production.

[a] *Department of Energy & Environmental Engineering, CSIR-Indian Institute of Chemical Technology, Tarnaka, Hyderabad, Telangana-500007, India. E-mail: upal03@gmail.com*

[b] *Academy of Scientific & Innovative Research (AcSIR), Ghaziabad, Uttar Pradesh-201002, India*

[c] *Department of Organic Synthesis and Process Chemistry, CSIR-Indian Institute of Chemical Technology, Hyderabad 500007, India. E-mail: ajaysingh015@gmail.com, ajaysingh015@iict.res.in*

† Electronic supplementary information (ESI) available. See DOI: https://doi.org/10.1039/d4cc05008h

This journal is © The Royal Society of Chemistry 2024

Published on 06 November 2024. Downloaded on 11/20/2025 5:27:09 PM.

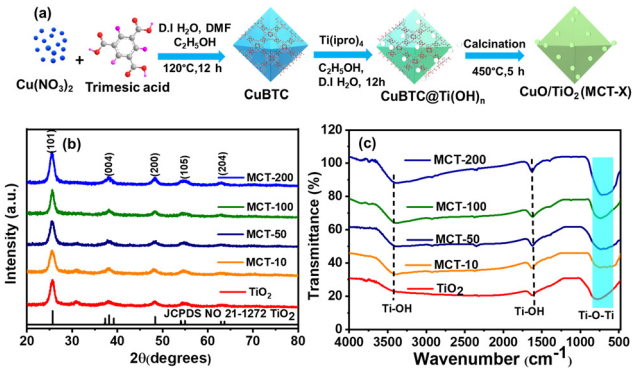

Fig. 1 (a) Schematic synthesis of the MCT-*X* composites, (b) XRD patterns and (c) FTIR of the as-synthesised photocatalysts.

To keep all these things in our mind we have started to develop the synthesis protocols for CuBTC, MOF-derived CuO/TiO_2 (MCT) and TiO_2 catalysts (details in the ESI†). Mesoporous CuO/TiO_2 catalysts were obtained *via* calcination at 450 °C in nitrogen, as shown in Fig. 1a. The XRD patterns of the as synthesised CuBTC (Fig. S1, ESI†), TiO_2 and MCT-*X* (where *X* = 10, 50, 100, and 200 mg of CuBTC) corresponding to MCT-10, MCT-50, MCT-100, and MCT-200 are shown in Fig. 1b. The main diffraction peaks align well with anatase TiO_2 (JCPDS no. 21-1272). No additional peaks for CuO, Cu_2O, or metallic Cu are observed, suggesting that CuO is highly dispersed on the TiO_2 surface, forming very small heterojunctions that do not significantly alter the TiO_2 crystal structure.[24] The FTIR spectra of TiO_2 and MCT-*X* nanoparticles show characteristic Ti–O–Ti bands (500–1000 cm^{-1}) and peaks for adsorbed water and hydroxyl groups (3435 cm^{-1}, 1632 cm^{-1}), as shown in Fig. 1c. With increasing CuO concentration, the peak intensities rise without new peaks emerging indicating CuO/TiO_2 interfacial bonding. These results corroborate XRD findings. The copper content in the MCT-*X* composites is found by ICP-MS (Table S1, ESI†).[25] XPS spectra were recorded to analyse the chemical structures and compositions of the synthesized catalysts. The survey spectra of TiO_2 and MCT-100 (Fig. S2a, ESI†) confirm the presence of Ti and O elements in TiO_2, and Ti, O, and Cu elements in MCT-100. The C 1s peak at 284.6 eV is attributed to residual carbon from the XPS instrument. The O 1s spectra of TiO_2 and MCT-100 (Fig. S2b, ESI†) were deconvoluted into three components: lattice oxygen (529.58–529.76 eV), surface hydroxyl groups (529.98–530.14 eV), and adsorbed water (531.26–531.73 eV). Hydroxyl groups can form active radicals, enhancing photocatalytic activity. MCT-100 showed a slight O 1s peak shift to higher binding energies, indicating reduced electronic density.[26] The Ti 2p XPS spectra in TiO_2 (Fig. S2c, ESI†) show peaks at 458.43 eV ($2p_{3/2}$) and 464.19 eV ($2p_{1/2}$), with 5.82 eV indicative of the Ti^{4+} oxidation state. In MCT-100 catalysts, these peaks shift slightly to 458.72 eV and 464.54 eV, respectively. These shifts suggest distinct TiO_2 entities and variation in the electronic state of Ti within Ti–O bonds. The absence of additional peaks in MCT-100 spectra implies CuO incorporation without TiO_2 lattice disruption, supporting electron transport at the CuO/TiO_2 heterojunction.[27] Cu 2p XPS spectra (Fig. S2d, ESI†) of MCT-100 revealed two characteristic peaks at binding energies of 952 eV ($2p_{1/2}$) and 932 eV ($2p_{3/2}$), with a separation of 20 eV and the shake-up satellite peak at 942.8 eV is indicative of the presence of predominant Cu^{2+} species. The EPR results are given in Fig. S3, ESI.†

The photocatalytic activities of the designed samples were examined for CO_2 reduction experiments under visible light using a 420 W Xe lamp in DMF (7 mL) + water (1 mL) solution. The results depicted in Fig. 2a showcase the methanol rates from TiO_2 and various MCT-*X* composites. The TiO_2 demonstrated a methanol production rate of 64 μmol g^{-1} h^{-1}. In contrast, the MOF-templated composites (MCT-*X*) exhibited substantially enhanced methanol generation. We observed that methanol production increased in relationship with higher CuO content obtained from MOF. The optimal performance was achieved with MCT-100, where 100 mg of CuBTC was used resulting in a methanol rate of 842 μmol g^{-1} h^{-1} over a 4 hour period. The quantum efficiency of the MCT-100 reaches 8.35% at 420 ± 20 nm wavelength. The further increasing of the CuBTC content in the MOF templated TiO_2 (MCT-200) decreases the methanol production activity. This might be the result of an excess of CuO covering the active sites on the TiO_2 surface and shielding the incident light from causing an electron transition. The absence of methanol in the dark indicates that the reaction is light-induced. Table S2 (ESI†) illustrates the comparison of the methanol production activity of the as-synthesized photocatalysts in the present work. The catalyst recycling experiments over four cycles are shown in Fig. S4, ESI.†

To evaluate how AI-enhanced flow chemistry improves methanol production, we conducted experiments after connecting all neural network and flow setups. We employed a closed-loop Bayesian optimization (BO) approach to investigate the effects of light intensity and residence time on reaction efficiency.

Our process involved using deionized water and hydrogen gas controlled by syringes and a mass flow controller, with parameters set *via* python code (detail in the ESI†) (Fig. 2b). The solution

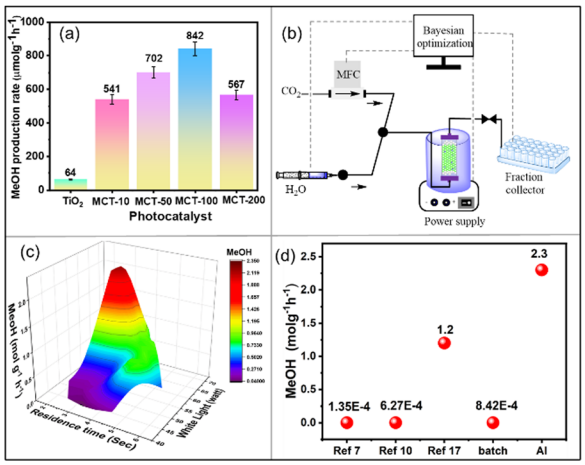

Fig. 2 (a) Methanol production rates of photocatalysts in batch mode, (b) schematic representation of the flow setup connected with AI, (c) the AI based system to auto-optimize and navigate this complexity and identify the optimal conditions for the photo activated methanol production, and (d) 2D graph comparing methanol production in batch and flow processes with the reference in the ESI.†

Published on 06 November 2024. Downloaded on 11/20/2025 5:27:09 PM.

mixing at a T-junction, and the gas–water mixture flowed through a PFA tubular reactor exposed to varying LED light wattages. Over 22 experiments in one day, the BO algorithm first explored the reaction conditions and then optimized them sequentially to maximize the yield. The optimized conditions for methanol production involved a deionized water flow rate of 0.26 mL min^{-1}, a carbon dioxide flow rate of 22 mL min^{-1}, exposure to a 64 ± 2 W LED light, a residence time of 2.7 s, and a pressure of 10 bar. Under these optimized conditions, we achieved an unprecedented methanol production rate of 2.3 mol g^{-1} h^{-1} (Fig. 2c). Notably, this rate surpasses those reported for batch processes by a remarkable factor of 2 to 100 times, highlighting the superior efficiency of our approach (Fig. 2d).

In our photocatalytic experiments, MOF-derived CuO/TiO_2 catalysts consistently demonstrated superior performance in methanol production compared to TiO_2 alone. To further investigate the structural effects of this integration, we analysed the UV-vis diffuse reflectance spectra (DRS) of the samples (Fig. 3a). The TiO_2 nanoparticles showed a prominent absorption band below 400 nm, indicating a 3.25 eV band gap. The Tauc plots of TiO_2, MOF-CuO and MCT-100 are given in Fig. S5 (ESI†). Introducing CuO nanoparticles in TiO_2 altered the absorption spectrum, adding a new peak in the 400–800 nm range. Increasing copper loadings shifted this peak to longer wavelengths, with the band between 600 and 800 nm attributed to Cu^{2+} d–d transitions. This optical absorption confirms the presence of CuO in the MCT-*X* composites.[24] Photoluminescence (PL) studies were conducted to investigate the light-induced charge separation and transport efficiency in TiO_2 and MCT-*X* (CuO/TiO_2) heterojunctions, which are critical for photocatalytic performance (Fig. 3b). PL emission spectra excited at 380 nm revealed a peak at ∼480 nm. In these studies, lower PL intensity suggests reduced electron–hole recombination, which enhances photocatalytic activity. The TiO_2 exhibited high PL intensity suggesting rapid charge recombination. However, CuO modification of TiO_2 resulted in decreased PL intensity, indicating improved charge separation at the CuO/TiO_2 interface.[26] The average PL lifetime of MCT-100 is 1.11 ns, which is 0.9 ns shorter than that of the TiO_2 counterpart (1.2 ns), as shown in Fig. 3c. The fluorescence quenching and the reduced exciton lifetime in MCT-100 indicated a significantly faster charge transfer and higher charge separation rate in CuO/TiO_2 than those of TiO_2.[28]

To explore the interfacial transfer and separation of photon-generated charge carriers in the photocatalysts, we carried out photoelectrochemical (PEC) property tests on TiO_2 and MCT-100. The Nyquist plot (Fig. 3d) reveal a larger arc radius for TiO_2 compared to MCT-100. Generally, a smaller arc in the Nyquist plot indicates lower interfacial charge transfer resistance, promoting better charge carrier transfer and enhancing photocatalytic activity. This suggests that MCT-100 is a more efficient electron-conducting catalyst than TiO_2.[29] Linear sweep voltammetry (LSV) studies (Fig. S6a, ESI†) reveal that MCT-100 shows the fastest increase in current density, owing to its low overpotential. This reduced overpotential facilitates rapid photogenerated charge transfer in TiO_2, confirming the excellent CO_2 reduction activity of MCT-100.[30] The flat band potentials (E_{FB}) of MOF-derived CuO and TiO_2 were estimated using Mott–Schottky plots (Fig. 3e and f) to examine the band alignments of the catalysts. Both materials exhibited characteristics of n-type semiconductors, with CuO and TiO_2 showing E_{FB} values of −0.56 V and −0.67 V *vs.* SCE, respectively. By using formula $E_{NHE} = E_{SCE} + 0.241$ and assuming that the conduction band (E_{CB}) is ∼0.2 negative to the E_{FB} in n-type semiconductors,[31] the E_{CB} values were calculated as −0.51 V (CuO) and −0.62 V (TiO_2) *vs.* NHE.[26] Combining these results with UV-DRS data and the relationship $E_{CB} = E_{VB} - E_g$, the valence band potentials (E_{VB}) were determined to be 1.31 V (CuO) and 2.62 V (TiO_2) *vs.* NHE. The more negative E_{CB} of TiO_2 compared to MOF-CuO indicates that photogenerated electrons can move from TiO_2 to CuO, promoting the separation of photogenerated electron–hole pairs. Photocurrent response analysis of TiO_2 and MCT-100 (Fig. S6b, ESI†) under periodic visible light illumination reveals enhanced charge carrier dynamics in the CuO/TiO_2 composite. MCT-100 exhibits higher photocurrent density than pristine TiO_2, attributed to efficient electron transfer from TiO_2 to CuO.[32,33] This PEC data confirms the formation of effective CuO/TiO_2 heterojunctions, enhancing photocatalytic performance in CO_2 reduction. The HRTEM (Fig. S7, ESI†) and BET (Fig. S8, ESI†) results are discussed in the ESI.†

Based on the band alignments derived from Tauc plots (Fig. S5, ESI†) and Mott–Schottky plots (Fig. 3e and f), a plausible mechanism for the photocatalytic reduction of CO_2 to methanol over the CuO/TiO_2 heterostructure can be proposed, as illustrated in Fig. 4. The conduction band (CB) of TiO_2 is positioned at a more negative potential relative to the CB of CuO, while the valence band (VB) of TiO_2 is at a more positive potential than the VB of CuO, forming a type-I heterojunction. Under light

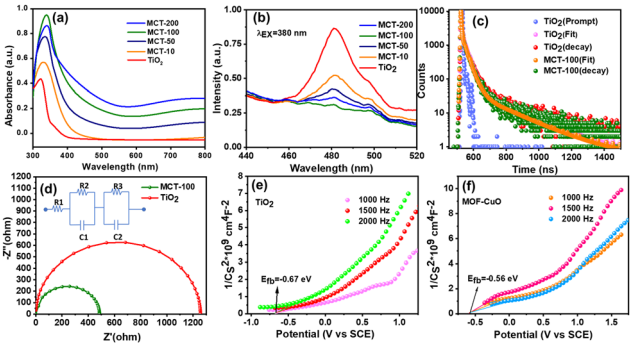

Fig. 3 (a) UV-DRS plots, (b) PL spectra of TiO_2 and MCT-*X*, (c) TCSPC spectra of TiO_2 and MCT-100, and (d) EIS plot of TiO_2 and MCT-100. Mott–Schottky plots of (e) MOF-CuO and (f) TiO_2.

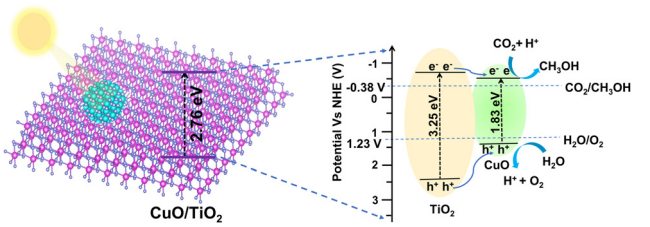

Fig. 4 Plausible mechanism for photocatalytic conversion of CO_2 to methanol through CuO/TiO_2.

 This journal is © The Royal Society of Chemistry 2024

Published on 06 November 2024. Downloaded on 11/20/2025 5:27:09 PM.

irradiation, both CuO and TiO_2 generate photogenerated electron–hole pairs. The electrons in the CB of TiO_2 are transferred to the CB of CuO, while the holes in the VB of TiO_2 migrate to the VB of CuO. The accumulated electrons in the CB of CuO act as reducing agents, participating in the multi-step reduction of adsorbed CO_2 molecules to methanol at catalytic sites on the CuO surface. Simultaneously, the holes concentrated in the VB of CuO facilitate the oxidation of water molecules, generating H^+ ions essential for the CO_2 reduction process. The formation of the type-I heterojunction effectively suppresses the recombination of photogenerated electrons and holes, promoting efficient charge separation and migration, thus enhancing the surface redox reactions that favour the photocatalytic reduction of CO_2 to methanol.

In summary, a noble metal-free, MOF-derived CuO/TiO_2 photocatalyst efficiently reduced CO_2 to methanol under visible light. Homogeneous dispersion of CuO in the heterojunction photocatalyst enhanced the photoreduction activity compared to TiO_2. The optimal composition, MCT-100, achieved the highest rate of 842 μmol g^{-1} h^{-1} in batch mode and 2.3 mol g^{-1} h^{-1} in a self-designed automated flow reactor under a fully light-driven process.

This work was supported by the HPCL (project no. CLP-0138/HPCL) and DST INSPIRE FELLOWSHIP (IF 220088). B. J., R. C., and A. R. thank DST for research funding and AcSIR for their PhD Enrolment. We are thankful to Dr D. Srinivasa Reddy, Director, CSIR-IICT for all research facilities. CSIR-IICT Communication no. IICT/Pubs./2024/342.

Data availability

The data supporting this article have been included as part of the ESI.†

Conflicts of interest

There are no conflicts to declare.

Notes and references

1 X. Ding, W. Liu, J. Zhao, L. Wang and Z. Zou, *Adv. Mater.*, 2024, 2312093, DOI: 10.1002/adma.202312093.
2 A. Kumar, P. K. Prajapati, U. Pal and S. L. Jain, *ACS Sustainable Chem. Eng.*, 2018, **6**, 8201–8211.
3 Y. A. Wu, I. McNulty, C. Liu, K. C. Lau, Q. Liu, A. P. Paulikas, C.-J. Sun, Z. Cai, J. R. Guest, Y. Ren, V. Stamenkovic, L. A. Curtiss, Y. Liu and T. Rajh, *Nat. Energy*, 2019, **4**, 957–968.
4 P. Huang, E. Shaaban, E. Ahmad, A. S. John, T. Jin and G. Li, *Chem. Commun.*, 2023, **59**, 9301–9319.
5 A. Tiwari, A. Goutam, S. Sk, P. Vijayanand, B. M. Abraham and U. Pal, *Int. J. Hydrogen Energy*, 2023, **48**, 29178–29188.
6 F. Han, H. Liu, W. Cheng and Q. Xu, *RSC Adv.*, 2020, **10**, 33620–33627.
7 S. D. Kshirsagar, S. P. Shelake, B. Biswas, K. Ramesh, R. Gaur, B. M. Abraham, A. V. S. Sainath and U. J. S. Pal, *Small*, 2024, 2407318, DOI: 10.1002/smll.202407318.
8 C. S. Vennapoosa, V. Tejavath, Y. T. Prabhu, A. Tiwari, B. M. Abraham, V. S. Upadhyayula and U. Pal, *J. CO_2 Util.*, 2023, **67**, 102332.
9 A. Gautam, S. Sk, A. Tiwari, B. M. Abraham, V. Perupogu and U. Pal, *Chem. Commun.*, 2021, **57**, 8660–8663.
10 Q. Guo, C. Zhou, Z. Ma and X. Yang, *Adv. Mater.*, 2019, **31**, 1901997.
11 I. Mondal, S. Gonuguntla and U. Pal, *J. Phys. Chem. C*, 2019, **123**, 26073–26081.
12 I. Mondal and U. Pal, *Phys. Chem. Chem. Phys.*, 2016, **18**, 4780–4788.
13 P. Ganji, R. K. Chowdari and B. Likozar, *Energy Fuels*, 2023, **37**, 7577–7602.
14 C. S. Vennapoosa, S. Varangane, B. M. Abraham, V. Bhasin, S. Bhattacharyya, X. Wang, U. Pal and D. Chatterjee, *J. Phys. Chem. Lett.*, 2023, **14**, 11400–11411.
15 J. Ding, Q. Tang, Y. Fu, Y. Zhang, J. Hu, T. Li, Q. Zhong, M. Fan and H. H. Kung, *J. Am. Chem. Soc.*, 2022, **144**, 9576–9585.
16 A. Kumar, K. K. Pant, S. Upadhyayula and H. Kodamana, *ACS Omega*, 2023, **8**, 410–421.
17 A. Slattery, Z. Wen, P. Tenblad, J. Sanjosé-Orduna, D. Pintossi, T. den Hartog and T. Noël, *Science*, 2024, **383**, eadj1817.
18 C. J. Taylor, A. Pomberger, K. C. Felton, R. Grainger, M. Barecka, T. W. Chamberlain, R. A. Bourne, C. N. Johnson and A. A. Lapkin, *Chem. Rev.*, 2023, **123**, 3089–3126.
19 D. Aand, A. Rana, A. Mottafegh, D. P. Kim and A. K. Singh, *React. Chem. Eng.*, 2024, **9**, 2427–2435.
20 A. D. Clayton, E. O. Pyzer-Knapp, M. Purdie, M. F. Jones, A. Barthelme, J. Pavey, N. Kapur, T. W. Chamberlain, A. J. Blacker and R. A. Bourne, *Angew. Chem., Int. Ed.*, 2023, **62**, e202214511.
21 T. M. Kohl, Y. Zuo, B. W. Muir, C. H. Hornung, A. Polyzos, Y. Zhu, X. Wang and D. L. J. Alexander, *React. Chem. Eng.*, 2024, **9**, 872–882.
22 G. Luo, X. Yang, W. Su, T. Qi, Q. Xu and A. Su, *Chem. Eng. Sci.*, 2024, **298**, 120434.
23 A. Mottafegh, G.-N. Ahn and D.-P. Kim, *Lab Chip*, 2023, **23**, 1613–1621.
24 Q. Shi, G. Ping, X. Wang, H. Xu, J. Li, J. Cui, H. Abroshan, H. Ding and G. Li, *J. Mater. Chem. A*, 2019, **7**, 2253–2260.
25 B. Rajamannan, S. Mugundan, G. Viruthagiri, P. Praveen and N. Shanmugam, *Spectrochim. Acta, Part A*, 2014, **118**, 651–656.
26 Y.-S. Ouyang, S.-T. Zheng, G.-W. Guan and Q.-Y. Yang, *ACS ACS Appl. Energy Mater.*, 2022, **5**, 14455–14465.
27 H. Hamad, M. M. Elsenety, W. Sadik, A.-G. El-Demerdash, A. Nashed, A. Mostafa and S. Elyamny, *Sci. Rep.*, 2022, **12**, 2217.
28 Z. Zeng, H. Yu, X. Quan, S. Chen and S. Zhang, *Appl. Catal., B*, 2018, **227**, 153–160.
29 R. Wang, J. Cao, J. Liu and Y. Zhang, *Int. J. Electrochem. Sci.*, 2023, **18**, 100316.
30 Y. Lu, H. Cao, S. Xu, C. Jia and G. Zheng, *RSC Adv.*, 2021, **11**, 21805–21812.
31 X. Wang, X. Wang, J. Huang, S. Li, A. Meng and Z. Li, *Nat. Commun.*, 2021, **12**, 4112.
32 D. Ni, H. Shen, H. Li, Y. Ma and T. Zhai, *Appl. Surf. Sci.*, 2017, **409**, 241–249.
33 H. Zhuang, S. Zhang, M. Lin, L. Lin, Z. Cai and W. Xu, *Mater. Adv.*, 2020, **1**, 767–773.